ACS Biomaterials SCIENCE & ENGINEERING

pubs.acs.org/journal/abseba
Article

Self-Powered Oxygen Microbubble Generator for Decontamination of Anaerobic Biofilm-Fouled Bioimplants

Eun-Hyuk Lee,[#] Hyunsub Kim,[#] Joo Hun Lee, Youngjoon Kim, Ho-Beom Kwon, Young-Jun Lim, Hyunjoon Kong,* Sang-woo Lee,* and Myung-Joo Kim*

Cite This: ACS Biomater. Sci. Eng. 2025, 11, 3019−3030

ABSTRACT: Biomedical devices often feature a microgap: confined, minuscule spaces that foster bacterial infiltration and biofilm formation. For instance, peri-implantitis with prevalence rates of 4.7−45% at the patient level is a major complication driven by biofilm infections, characterized by chronic inflammation and implant failure. Anaerobic biofilm residing within the microgap serves as a major source of the peri-implantitis, but tools that remove the biofilm are lacking. Therefore, this study presents a novel preventive strategy employing **s**elf-powered **m**icrobubbler (SM) for targeted decontamination of micrographs in dental implants. SMs are assembled by doping diatoms with MnO_2 nanosheets. These particles are activated to generate O_2 microbubbles in H_2O_2 solution via catalase-mimetic activity and can penetrate the biofilm structures. The resulting oxygen bubbles induce effective mechanical disruption and oxygenation within biofilm-mimicking gelatin hydrogels and *Porphyromonas gingivalis* biofilms found in the peri-implantitis-affected implants. Such biofilm removal from the microgap restored mechanical stability at implant abutment-fixture connections and reduced bacterial leakage. Multispecies biofilms from patient-derived implants were similarly decontaminated with the mixture of SM-H_2O_2 outperforming conventional antiseptics like 0.2% chlorhexidine and 3% H_2O_2 alone. This innovative approach extends beyond dental implants to address biofilm-associated challenges in various biomedical devices with microgap vulnerabilities. Overall, SM-based treatments will offer an efficient and nondamaging solution to enhance the sterility and longevity of various bioimplants with intricated and confined structure.

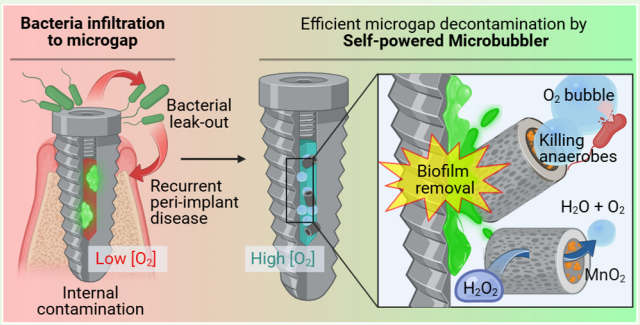

KEYWORDS: *microgap, decontamination, nanozyme, dental implants, biofilms, manganese oxide, diatoms*

INTRODUCTION

Biofilms, characterized by their extracellular polymeric substance (EPS) matrix, confer resistance to antimicrobials and host immune responses, significantly complicating treatment.[1] Biofilm formation in medical devices poses severe clinical and economic burdens. For instance, urinary catheters are often colonized by *Escherichia coli* and *Proteus mirabilis*, leading to catheter-associated urinary tract infections,[2] while articular components of orthopedic implants are susceptible to *Staphylococcus aureus*, contributing to implant-associated osteomyelitis.[3] Similarly, pocket and leads of pacemaker face colonization by *S. aureus*, resulting in device-related endocarditis.[4] Dental implants present a unique challenge due to their structural design. The fixture-abutment interface (FAI) in two-piece bone-level internal implants often harbors microgaps, which allow bacterial infiltration and biofilm accumulation, leading to peri-implant diseases and mechanical instability.[5,6] Among biomedical devices, dental implants exhibit the highest infection rates, with biofilm-related complications occurring in 5.9−56% of cases, compared to lower rates in prosthetic joints (1−15%), urinary catheters (9.1−26.6%), and cardiac devices (0.13−38.6%).[7] This underscores the critical need for innovative decontamination strategies that are tailored to these challenging environments.

Porphyromonas gingivalis, a dominant anaerobic pathogen in peri-implantitis, has been consistently implicated in inflammatory bone loss around implants, compromising their structural and functional integrity.[8] Conventional treatments, such as chemical antiseptics (e.g., 0.2% chlorhexidine gluconate, 3% hydrogen peroxide), fail to fully eradicate biofilms due to the protective EPS matrix.[9] Mechanical methods, including swabbing or irrigation, are similarly inadequate for difficult-to-access geometries of microgaps.[10] As a result, the persistent biofilm reservoirs within these confined spaces pose a significant risk of infection recurrence and mechanical failure.

Received: February 12, 2025
Revised: March 24, 2025
Accepted: April 14, 2025
Published: April 21, 2025

Scheme 1. Schematic Representation of Bacterial Infiltration via Implant Microgap, Synthesis of SM, and Microgap Biofilm Decontamination Using SM

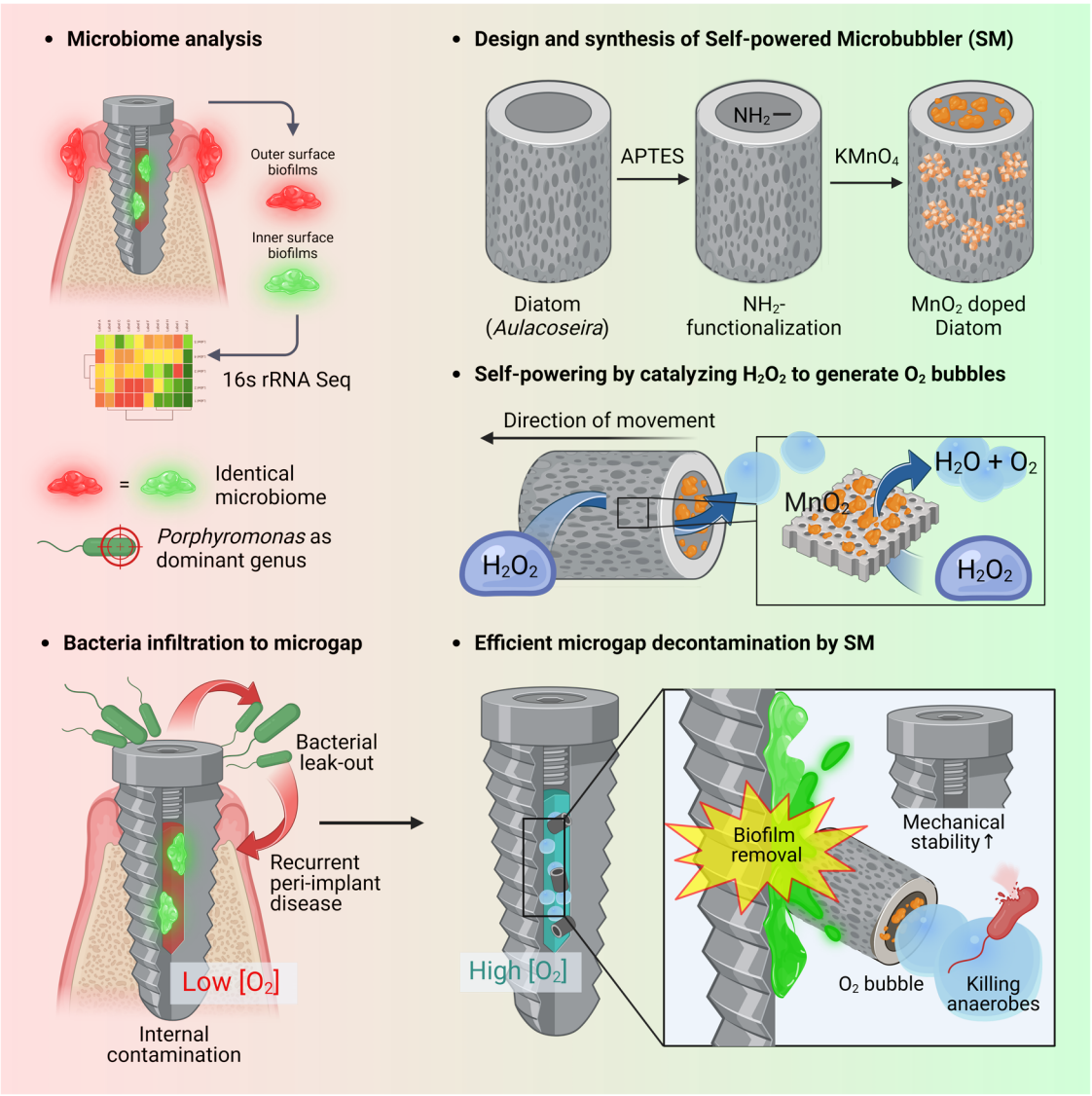

Emerging nanotechnology-based approaches, including antimicrobial peptides,[11,12] magnetically driven catalytic antimicrobial robots,[13] and photodynamic therapy,[14] have shown promise in mitigating biofilm formation, yet their efficacy in microgap environments remains limited. Biological and chemical approaches, including antimicrobial peptides, can induce bacterial death or inhibit growth, but are unable to remove extracellular polymeric substances (EPS) in microgap environments. Nano- to microsized robots have the potential to achieve both physical and chemical biofilm removal in microgaps, but their complex and costly synthesis processes make them impractical for industrial-scale applications.

To overcome these limitations, we propose the use of self-powered microbubblers (SM) to remove anaerobic biofilms in microgaps of biomedical devices, particularly dental implants, through a combination of mechanical abrasion and oxygenation. These SM are fabricated by doping cylindrical, porous diatom particles with MnO_2 nanosheets by reducing $KMnO_4$ precursor on the amine-substituted diatoms. This design enables SMs to penetrate the biofilm by generating oxygen bubbles in hydrogen peroxide (H_2O_2) solution (Scheme 1). Such bubble-driven propulsion of rigid diatoms leads to simultaneous physical disruption and oxygenation of anaerobic niches (Scheme 1). This dual capability is not achievable using free MnO_2 nanosheets or particles alone. The efficacy of SMs was evaluated under various *in vitro* and *ex vivo* conditions, closely mimicking clinical settings. Our study demonstrates the efficacy of SM technology in eliminating biofilms from dental implant microgaps and highlights its potential for broader application across biomedical devices with confined microstructures.

MATERIALS AND METHODS

Patient-Derived Implant Fixtures and Related Ethics Statement. All patient-derived implant fixtures used in this study were extracted for therapeutic purposes. Those implants were severely affected by peri-implantitis and showed periapical radiolucency, a more than 6 mm pocket depth, or severe mobility. This study was approved by the Ethics Committee of the Seoul National University Dental Hospital (IRB136-10-19).

16s rRNA Sequencing-Based Microbiome Analysis. For the inner surface sampling, 20 μL of Trizol (Invitrogen; Thermo Fisher Scientific, Inc.) was loaded into the internal spaces of implants and

https://doi.org/10.1021/acsbiomaterials.5c00303
ACS Biomater. Sci. Eng. 2025, 11, 3019−3030

pipetted at least 10 times; 200 μL of Trizol was repetitively dripped on the outer implant surfaces for outer surface sampling. DNA was extracted using DNeasy PowerSoil Kit (Qiagen) according to the manufacturer's protocol. The extracted DNA was quantified using a Quant-IT PicoGreen (Invitrogen; Thermo Fisher Scientific, Inc.). Each sequenced sample was prepared following the Illumina 16S Metagenomic Sequencing Library protocols to amplify the V3 and V4 regions. The paired-end (2 × 300 bp) sequencing was performed using the MiSeq sequencer (Illumina).

Library Preparation and 16s rRNA Sequencing for Microbiome Analysis. Each sequenced sample is prepared according to the Illumina 16S Metagenomic Sequencing Library protocols to amplify the V3 and V4 regions. The input gDNA 5 ng was PCR amplified with 5× reaction buffer, 1 mM dNTP mix, 500 nM each of the universal F/R PCR primer, and Herculase II fusion DNA polymerase (Agilent Technologies, Santa Clara, CA). The cycle condition for first PCR was 3 min at 95 °C for heat activation and 25 cycles of 30 s at 95 °C, 30 s at 55 °C, and 30 s at 72 °C, followed by a 5 min final extension at 72 °C. The universal primer pair with Illumina adapter overhang sequences used for the first amplifications were as follows:

V3-F: 5′-TCGTCGGCAGCGTCAGATGTGTATAAGAGACAGCCTACGGGNGGCWGCAG-3′.

V4-R: 5′-GTCTCGTGGGCTCGGAGATGTGTATAAGAGACAGGACTACHVGGGTATCTAATCC-3′.

The first PCR product was purified with AMPure beads (Agencourt Bioscience, Beverly, MA). Following purification, 2 μL of first PCR product was PCR amplified for final library construction containing the index using Nextera XT Indexed Primer. The cycle condition for the second PCR was the same as the first PCR condition except for 10 cycles. The PCR product was purified with AMPure beads. To achieve the highest quality of data on Illumina sequencing platforms, it is important to create optimum cluster densities across every lane of the flow cell. This requires accurate quantification of DNA library templates, and therefore, we quantified prepared libraries using qPCR following the Illumina qPCR Quantification Protocol Guide (KAPA Library Quantification kits for Illumina Sequencing platforms) and qualified using the TapeStation D1000 ScreenTape (Agilent Technologies, Waldbronn, Germany). The paired-end (2 × 300 bp) sequencing was performed using the MiSeq sequencer (Illumina, San Diego).

Data Analysis for Microbiome Analysis. The paired-end method generated fastq files that are converted into QIIME2 artifacts, which are available for further analysis. Demultiplexed data was processed using the DADA2 algorithm, including error correction and removal of rare taxa, to generate representative sequences and a feature table. The microbial classification of each representative sequence was confirmed by blasting against the 16s rRNA gene database. The Q2-Feature classifier is a Naive Bayes classifier trained based on the SILVA reference (region V3−V4) database (https://www.arb-silva.de/) to classify the data set used in the experiment. A resultant table was then used to generate a phylogenetic tree for downstream α and β analysis. The "core metrics analysis" command was used to generate Shannon diversity index and phylogenic diversity index. ANCOM analysis was used to verify and visualize the differences in the feature composition between groups.

Synthesis of MnO_2 Nanozyme-Doped Diatoms. To prepare MnO_2-doped diatoms, we followed the method used in a previous study.[15] Briefly, to synthesize amine-substituted diatoms, 2 g of diatoms, 60 mL of toluene (Sigma-Aldrich), and 0.6 mL of distilled water (DDW) were mixed with a magnetic stirrer at room temperature for 2 h. After that, 3.4 mL of (3-aminopropyl) triethoxysilane (APTES; Sigma-Aldrich) was added, and the mixture was heated to 60 °C and refluxed for 6 h. After the cool-down, the mixture was sequentially washed with toluene, 2-propanol (Sigma-Aldrich), and DDW. After drying in a vacuum desiccator for 2 days, 0.1 g of the amine-substituted diatoms was reacted with 1 mL of 50 mM potassium permanganate ($KMnO_4$; Sigma-Aldrich). The resulting MnO_2-doped diatoms were rinsed with DDW and ethanol and then dried for 24 h at 60 °C.

Physicochemical Characterization of SMs. To investigate the physicochemical properties of the prepared SMs, we obtained scanning electron microscopy (SEM) images using an Apreo S microscope (Thermo Fisher Scientific) at magnifications of 15,000 and 50,000 times at 10.0 kV. We also used an energy-dispersive spectrometer (EDS) in combination with SEM at 20.0 kV to conduct elemental analysis and confirm the successful doping of MnO_2 nanozyme onto the surface of the diatom particles. The catalytic activity of SM was estimated by measuring the O_2 gas generated from SM + 3% H_2O_2 (Sigma). 1, 2, 4, and 8 mg of SM was reacted with 1 mL of 3% H_2O_2 inside a 50 mL conical tube (SPL) for 1200 s, and the accumulated O_2 concentration present in air within the tube was measured using a gas sensor (Vernier).

Artificial Biofilm Removal Assay. Warmed up (80 °C) 6% w/v porcine gelatin (Sigma) solution was mixed with 1% v/v red food color. 20 μL of the mixture was placed inside internal spaces of sterile bone-level internal-type implants (diameter: 4.0 mm; length: 7.0 mm; Luna, Shinhung) and cooled down for 15 min at room temperature. After that, the implants were placed in microtubes upside down, and they were centrifuged at 5000 rpm for 1 s. Coating quality was confirmed with an ENT endoscopic visual system (V1 SMART mini, Donga Chammed), and poorly coated implants were discarded. After each treatment (20 μL of PBS, 3% H_2O_2, and different amount of SM + 3% H_2O_2), implant internal spaces were washed twice with DDW, then imaged with the endoscope. Percentages of the artificial biofilm-coated area were calculated by ImageJ.

Biofilm Formation on the Inner Surface of Implants. Sterile bone-level internal-type implants (Luna, Shinhung) were placed in a 48-well tissue culture plate and inoculated with 1 mL of a *P. gingivalis* (ATCC 33277) suspension to form biofilms. *P. gingivalis* was cultured in brain-heart infusion (BHI) broth (Becton, Dickinson, and Company) supplemented with 5.0 mg/mL hemin (Sigma) and 0.5 mg/mL vitamin K (Sigma). The bacterial concentration of *P. gingivalis* was adjusted to 2.0×10^8 CFU/mL, based on the standard curve of OD 600 nm versus CFU/mL for *P. gingivalis*. The implants inoculated with *P. gingivalis* were incubated in an anaerobic chamber (10% H_2, 10% CO_2, and balanced N_2) at 37 °C for 48 h. For the patient-derived multispecies biofilm culture and inoculation, biofilm was harvested from extracted peri-implantitis-affected implants by scraping off the internal spaces with sterilized pipet tips. The harvested biofilm was transferred to the internal space of sterilized implants and cultured following the protocol of *P. gingivalis* culture (mentioned above).

Bacterial Viability Assay. Fifty sterile bone-level internal-type implants were randomly divided into five groups (n = 10). The negative control group received implants in 1 mL of sterile broth, while the other four groups were inoculated with *P. gingivalis* to create biofilms using a previously described method. After 48 h, the implants were rinsed with phosphate-buffered saline (PBS, pH = 7.4). The implants with biofilms were then treated with 20 μL of PBS (PBS group), 0.12% (w/v) Chlorhexidine (CHX) (Bukwang Pharmaceutical Co., Ltd., Seoul, Korea) (CHX group), 3% (v/v) H_2O_2 (H_2O_2; Sigma-Aldrich, St. Louis, MO) (H_2O_2 group), or cotreatment with 4 mg of SM and 3% H_2O_2 (SM + H_2O_2 group) for 2 min.

The treated implants were then rinsed with PBS before being placed in a 96-well tissue culture plate. The dimensions of this tissue culture plate were suitable for the comfortable placement of the implants for subsequent experiments. To assess the viability of the remaining bacteria, 190 μL of sterile BHI broth and 10 μL of cell counting kit-8 (CCK-8) solution (Dojindo Laboratory, Kumamoto, Japan) were added to another 96-well tissue culture plate. Using a pipet, 20 μL of the BHI broth and CCK-8 solution mixture was added to the internal cavity of the implants. The bacterial suspension was then pipetted and transferred back to the mixture every 30 min during a 2 h incubation period at 37 °C. The colored mixture was examined through bright-field imaging using a stereomicroscope (Leica S6D, Leica Microsystems, Wetzlar, Germany), and its absorbance at 450 nm was measured by a microplate reader (Epoch 2, Bio-Tek Instruments, Winooski, VT).

https://doi.org/10.1021/acsbiomaterials.5c00303
ACS Biomater. Sci. Eng. 2025, 11, 3019−3030

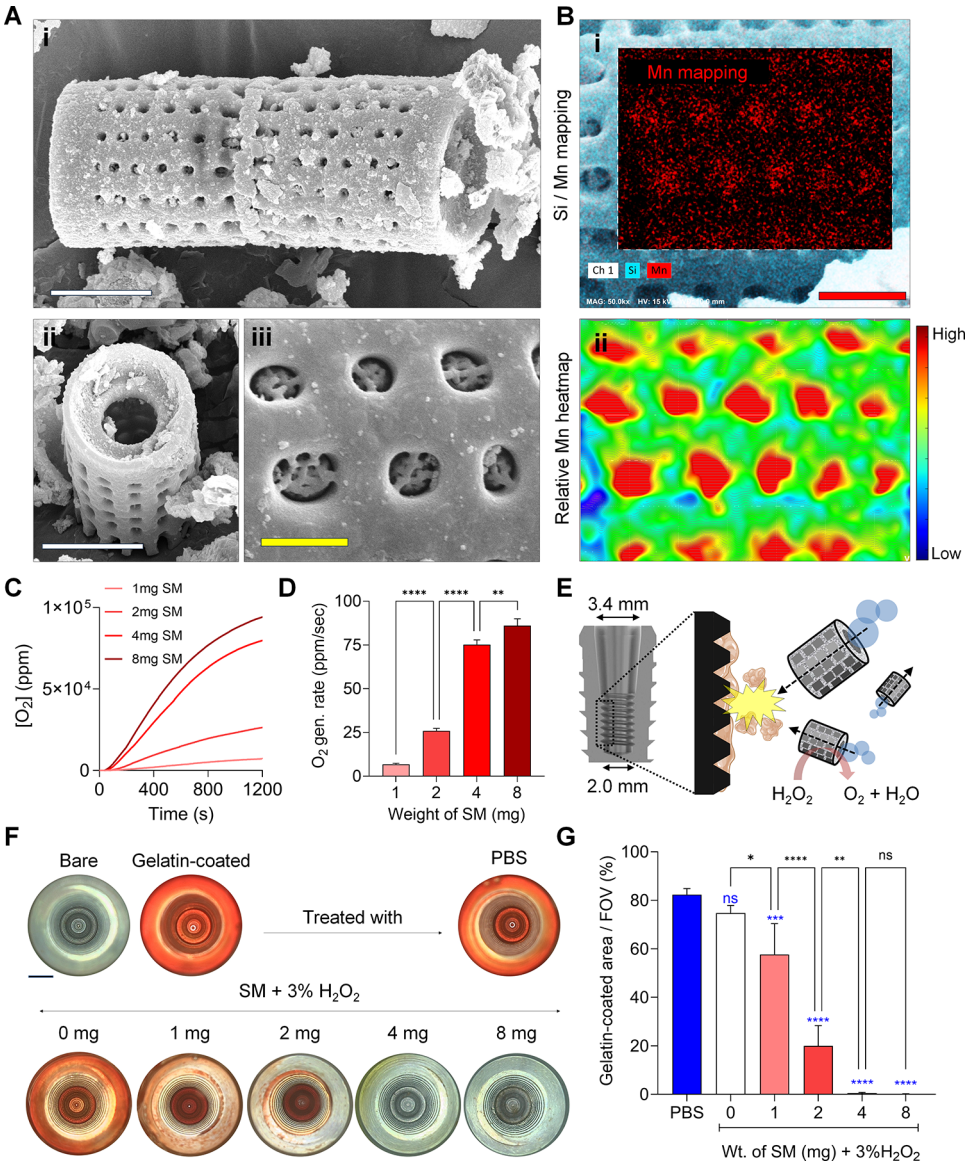

Figure 1. Physicochemical characterization of SM. (A) SEM images of SM (panels (i), (ii)) and alveolae (panel (iii)). White scale bar = 10 μm, yellow scale bar = 1 μm. (B) EDS element mapping of SM (panel (i)) and relative Mn heat map (panel (ii)). Red scale bar = 800 nm. (C) Quantification of O_2 gas generated from 3% H_2O_2 solution mixed with varying amounts of the MnO_2-diatom bubbler. (D) Quantification of O_2 production rate generated from 3% H_2O_2 solution mixed with varying amounts of the MnO_2-diatom bubbler. Data are expressed as average ± standard error of the mean (s.e.m.). Statistical significance was set to $^{**}p < 0.01$, $^{****}p < 0.001$. (E) Schematic diagram of SM decontaminating the inner surface of the implant. (F) Artificial biofilm removal test treated with 3% H_2O_2 solution mixed with varying amounts of the MnO_2-diatom bubbler. Scale bar = 2 mm. (G) Relative quantification of the remaining artificial biofilm after treatment of H_2O_2 + SM. Data are expressed as average ± standard error of the mean (s.e.m.). Significance is set to ns, not specific; $^{*}p < 0.05$, $^{**}p < 0.01$, $^{***}p \leq 0.001$, $^{****}p \leq 0.0001$.

SEM Analysis. The biofilms remaining on the inner surface of cross-sectioned implants were observed using SEM (Apreo S; Thermo Fisher Scientific, Waltham, MA) after each treatment. The specimens were rinsed with PBS and then fixed with 1 mL of 2.5% (v/v) glutaraldehyde for 4 h. After fixation, the specimens were washed with PBS and dehydrated using a series of ethanol solutions (50, 70, 95, and 100%). Once the specimens had dried completely, they were coated with platinum and visualized using SEM at a voltage of 10 kV to observe the biofilms. The number of bacteria within a 100 μm^2 area in the SEM images was measured.

Inner Surface Decontamination Assay on Implants Extracted from Patients. Internal spaces of implant fixtures extracted from patients were stained with a disclosing agent (GC Tri Plaque ID Gel, GC America Inc.) and then washed twice with warm phosphate-buffered saline (PBS). The initial contamination status was captured by using an ENT endoscope. Subsequently, those fixtures were treated with 4 mg SM + 20 μL 3% H_2O_2 for 300 s. Decontamination progress was monitored at 30 s intervals using a stereoscope microscope (S90D, Leica). After the treatment, internal spaces were imaged again with an ENT endoscope. Contaminated areas were calculated using ImageJ.

CLSM Analysis. To assess viability, biofilms on the inner surface of cross-sectioned implants were washed with PBS after each treatment and stained with the Live/Dead BacLight viability kit, which contained SYTO-9 and propidium iodide (Invitrogen, Eugene, OR). The specimens were incubated with the staining solution in a dark cabinet for 20 min and then washed with PBS. The cross-sectioned implants were placed with their cut surfaces facing downward in the bottom of confocal dishes (SPL Life Science, Kyong-Gi, Korea) with BacLight mounting oil (Thermo Fisher Scientific, Waltham, MA). The stained biofilms were imaged by using

https://doi.org/10.1021/acsbiomaterials.5c00303
ACS Biomater. Sci. Eng. 2025, 11, 3019−3030

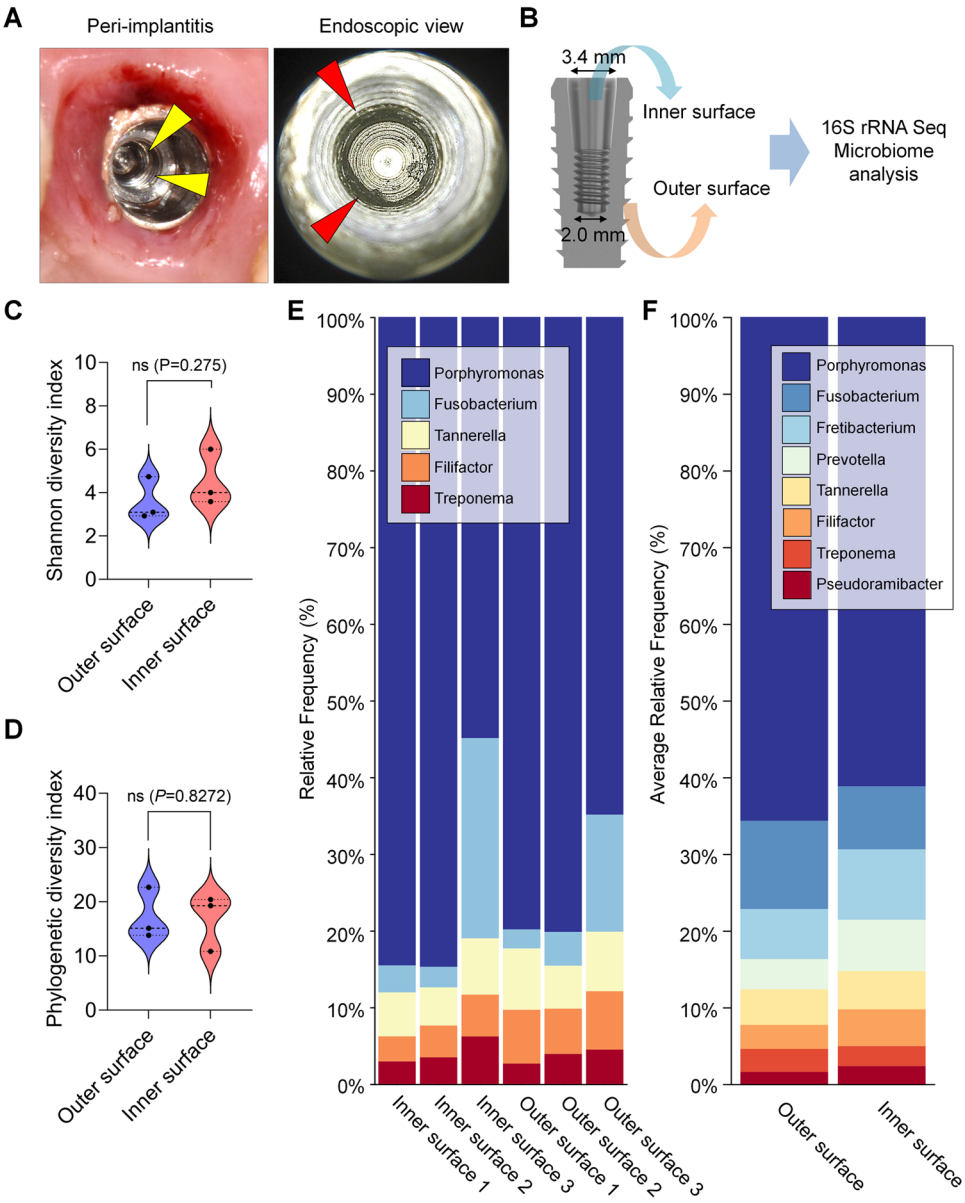

Figure 2. Microbiome analysis of bacteria on outer and inner surfaces of dental implants. (A) Clinical photo of peri-implantitis and endoscopic view of implant internal space. Implant internal space is marked with yellow arrow. Contaminated areas are marked with red arrow. (B) Schematic diagram of sample collection from inner and outer surfaces of implant. (C) Shannon diversity index of samples collected from outer and inner surfaces (n = 3). (D) Phylogenetic diversity index of samples collected from outer and inner surfaces (n = 3). (E) Relative frequencies of bacterial genus collected from outer and inner surfaces (n = 3). The relative abundance was set to 1%. (F) Average relative frequencies of bacterial genus collected from outer and inner surfaces (n = 3). The average abundance was set to 1%.

confocal laser scanning microscopy (CLSM) (LSM700; Carl Zeiss, Oberkochen, Germany).

Reverse Torque Test. After *P. gingivalis* biofilms are formed on inner surfaces of bone-level internal-type implants (Luna, Shinhung), they were treated by 20 μL of PBS, CHX, 3% H_2O_2, or 4 mg SM + 3% H_2O_2. After the treatment, the reverse torque value (RTV) was measured using the experimental procedures outlined in a previously published method.[16] Each implant was secured in a customized jig (Figure S2), and a 4.5 mm diameter, 3.0 mm gingival height Duo abutment (Luna, Shinhung) was connected to the implant. 30 N cm torque was applied to the prosthetic screw with a digital screw torque meter (MGT 50, MARK-10, Copiague). The implant abutment assemblies were then retightened with 30 Ncm torque after 10 min of embedment relaxation. Subsequently, the reverse torque values were measured by using the digital screw torque meter.

Bacteria Leakage Test. 2.0 × 10^8 CFU/mL *P. gingivalis* was inoculated to sterile bone-level internal-type implants (Luna, Shinhung) and incubated for 48 h. After the biofilm formation, each implant was treated with different substances (20 μL of PBS, CHX, 3% H_2O_2, and 4 mg of SM + 3% H_2O_2) within its internal space. After the treatments, implants were connected with Duo abutment (4.5 mm diameter, 3.0 mm gingival height, Luna, Shinhung) with 30 N cm torque. Outer surfaces of implants were sterilized with manual cleansing with 70% ethanol swap and 30 min of UV irradiation. Next, implants were immersed in 1 mL of *P. gingivalis* culture media and then incubated for 10 days. The bacterial leakage from the fixture-abutment interface was quantified by measuring the OD 600 nm of the culture media at 0, 4th, 7th, and 10th day using a microplate reader (Epoch 2; Bio-Tek Instruments).

Stained Biofilm Removal Assay. A total of 20 bone-level internal-type implants were embedded in an acrylic resin block

https://doi.org/10.1021/acsbiomaterials.5c00303
ACS Biomater. Sci. Eng. 2025, 11, 3019−3030

(Ortho-Jet; Lang Dental, Wheeling, IL) and cross-sectioned along their longitudinal axis (Figure S1a) using a cutting machine (Isomet 1000, Buehler, Lake Bluff, IL) (n = 5). The cross-sectioned implants were then reassembled to their original form using a flowable composite resin (Denfil Flow, Vericom, Anyang, Korea) and sterilized (Figure S1). To create biofilms on the inner surface of the implants, a previously described method was used. In order to stain the extracellular polymeric substance (EPS), the implants were placed in BHI broth containing 10 μg/mL of FITC-conjugated Concanavalin A (Sigma, St. Louis, MO) for 20 min in a dark cabinet at room temperature. After incubation, the implants underwent a PBS rinse, were reseparated, and then imaged using a fluorescence imaging system (FOBI; Neoscience, Suwon, Korea). The implants were then reassembled with flowable composite resin and placed in a 48-well tissue culture plate, with each group receiving appropriate treatment. Following a PBS wash, the implants were reseparated and imaged again using the fluorescence imaging system. The stained areas in cross-sectional images of the implants ("before treatment" and "after treatment") were measured using image analysis software (ImageJ; National Institutes of Health, Bethesda, MD).

Physicochemical Characteristics of the Titanium Disk Surface. The machined titanium disks (diameter: 10.0 mm; height: 1.0 mm; Dentium, Seoul, Korea) were treated with double distilled water (DW group), 3% (v/v) H_2O_2 (H_2O_2; Sigma-Aldrich, St. Louis, MO) (H_2O_2 group), cotreatment with DW and 4 mg of SM (DW + SM group) or cotreatment with 3% H_2O_2 and 4 mg of SM (SM + H_2O_2 group) for 4 min (n = 4). After each treatment, titanium disks were cleaned in an ultrasonic cleaner for 5 min and then gently wiped and air-dried before analysis. The chemical composition of the titanium disk surfaces was analyzed by using X-ray photoelectron spectroscopy (XPS, Axis Supra, Kratos, Manchester, U.K.) with monochromatic aluminum X-ray radiation (1486.6 eV). The binding energy scale was calibrated by using a reference peak of C 1s (BE = 284.5 eV). The surface roughness of the titanium disks after each treatment was measured by using confocal laser scanning microscopy (CLSM; LSM 800, Carl Zeiss, Jena, Germany). The average surface roughness (R_a) values were calculated over an area of 319 × 319 μm^2.

Statistical Analysis. The data were determined to follow a normal distribution based on the Shapiro–Wilk normality test (α = 0.05), and homogeneity of variance was assessed using Levene's test (α = 0.05). A statistical analysis was performed on the quantitative data obtained from the bacterial viability assay, SEM analysis, reverse torque test, and physicochemical characteristics of the titanium disk surfaces using one-way ANOVA, followed by Tukey's multiple comparison test (α = 0.05) as a post hoc test. The stained biofilm removal assay was analyzed using a two-way repeated-measures ANOVA test (α = 0.05). Pairwise comparisons of areas of stained biofilms before and after each treatment were conducted using the Bonferroni method (α = 0.05), and comparisons among groups were made using Tukey's multiple comparison test (α = 0.05) as a post hoc test. Statistical analyses were performed using Prism 9 (GraphPad, San Diego, CA).

RESULTS

Physicochemical Characterization of SM. The synthesized SM exhibited the typical morphological features of *Aulacoseria* diatoms, consisting of two 20-μm-long hollow cylindrical bodies connected by spines (Figure 1A, panels (i) and (ii)). Circular pores, known as alveolae, were linearly aligned on the main body of the diatom, with further microsized complex structures inside the alveolae (Figure 1A, panel (iii)), which exert strong capillary pressure to absorb liquids. EDS analysis confirmed successful doping of manganese on diatom surfaces, which were primarily composed of amorphous silica (Figure 1B). Manganese content was significantly higher in the microstructures of the alveolae (Figure 1B, panels (i) and (ii)), suggesting a greater likelihood of localized O_2 bubble generation within the inner cavity of the diatom body rather than on the surface.

The O_2 production rate serves as an indicator of catalytic activity and the kinetic energy of SM.[10] As the mass of SM mixed with 1 mL of 3% H_2O_2 increased from 1 to 8 mg, the cumulative O_2 concentration steadily rose over 800 s before slowing down (Figure 1C). A notable increase in the O_2 production rate occurred between 2 mg and 4 mg, but the rate became saturated above 4 mg, indicating that 4 mg was the optimal amount (Figure 1D).

To confirm the optimal amount of SM for internal decontamination of implants, varying amounts of SM were applied to remove gelatin-based artificial biofilms coated on the inner microstructures of the implants (Figure 1E). Neither PBS nor 3% H_2O_2 solution treatment alone was able to remove the artificial biofilms. However, cotreatment with SM and 3% H_2O_2 (SM + H_2O_2) effectively removed the artificial biofilms (Figure 1F,G). As expected, decontamination efficiency significantly increased from 2 to 4 mg, achieving complete removal of artificial biofilms, even from the deepest parts of the internal space (Figure 1F,G).

Microbiome Analysis of Bacteria on Outer and Inner Surfaces of Dental Implants. Next, to confirm whether bacteria can colonize the implant microstructure through the microgap, bacterial species on the outer and inner surfaces of peri-implantitis-affected dental implants were identified and compared using 16S rRNA sequencing. Endoscopic imaging of the implant's inner microstructure confirmed the presence of blackish bacterial biofilm at the deepest part of the internal space (Figure 2A). Bacterial genomes were directly collected from both inner and outer implant surfaces using Trizol, and 16S rRNA sequencing-based microbiome analysis was performed (Figure 2B). Based on a significant W threshold, among 692 bacterial species, no significant difference was observed between the bacterial species present on the inner and outer surfaces of the implants (0 true, 692 false).

According to the α diversity (Shannon diversity index) and β diversity (Phylogenetic diversity index), there was no significant difference in bacterial species diversity between the outer and inner surfaces (Kruskal–Wallis p = 0.275 and p = 0.8272, respectively; Figure 2C,D). The taxonomic bar plot reveals that the dominant bacterial genus on both the outer and inner implant surfaces is *Porphyromonas*, constituting more than 60% of the total bacterial genus on both surfaces (Figure 2E,F). Other genera, including *Fusobacterium*, *Fretibacterium*, *Prevotella*, *Tannerella*, *Filifactor*, *Treponema*, and *Pseudoramibacter*, followed *Porphyromonas* in abundance (Figure 2F). These results provide direct evidence that bacteria can freely pass through the microgap between the abutment and fixture, allowing the inner surface to serve as a reservoir for bacteria. Since we identified *Porphyromonas* as the dominant bacterial genus inhabiting the implant's internal microstructure, our subsequent *in vitro* experiments will be conducted using *P. gingivalis* biofilms.

Decontamination Efficiency of SM and Conventional Antiseptics on *P. gingivalis* Biofilms within the Inner Implant Microstructures. To compare the decontamination efficiencies of SM and conventional antiseptics for inner implant microstructures, bacterial viability assays, SEM imaging, and biofilm EPS visualization were performed after treatment with 4 mg of SM + 20 μL of H_2O_2, 3% H_2O_2 (H_2O_2), and CHX on *P. gingivalis* biofilms cultured inside the internal spaces of implants (Figure 3A). Bacterial viability

https://doi.org/10.1021/acsbiomaterials.5c00303
ACS Biomater. Sci. Eng. 2025, 11, 3019–3030

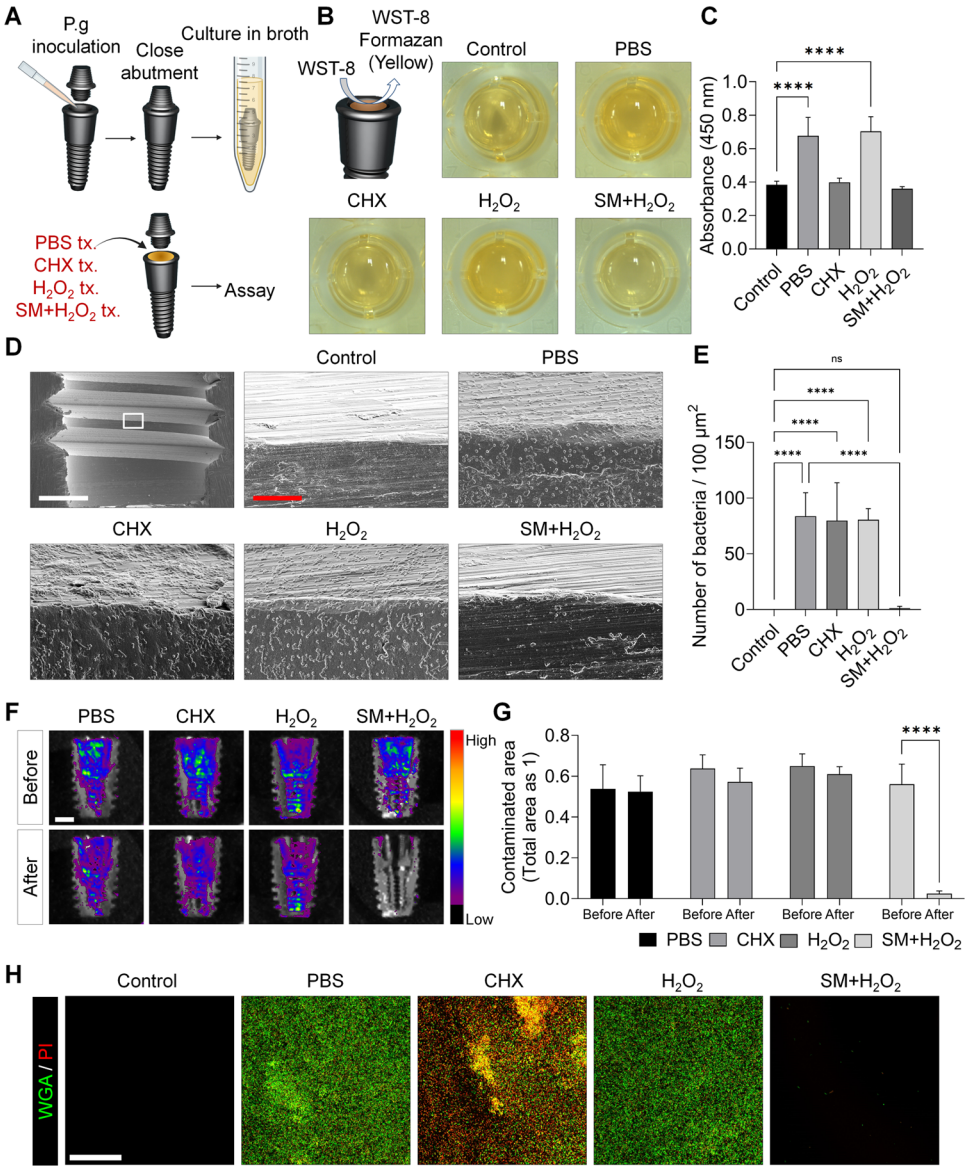

Figure 3. Inner implant microstructures decontamination efficiency of SM and conventional antiseptics on *P. gingivalis* biofilms. (A) Schematic illustration of the inoculation of *P. gingivalis* biofilms inside the internal surface of implants and the subsequent biofilm removal experiment. (B) Bacterial viability result after each treatment. Yellow WST-8 formazan indicates viable bacteria. (C) Absorbance of WST-8 formazan solutions at 450 nm in (B) is quantified (n = 10). Data are expressed as average ± standard error of the mean (s.e.m.). Significance is set to ****$p \leq 0.0001$. (D) SEM images of the inner surfaces of the implants after decontamination in 15,000 and 50,000×. White scale bar is 500 μm, and red scale bar is 10 nm. (E) Quantification of the number of bacteria within 100 μm^2 in (D). Data are expressed as average ± standard error of the mean (s.e.m.). Significance is set to ns, not specific; ****$p \leq 0.0001$. (F) Relative fluorescence heat map of Concanavalin A-FITC-stained biofilms before and after each treatment. Scale bar = 2 mm. (G) Stained areas in (F) are measured (n = 5). Data are expressed as average ± standard error of the mean (s.e.m.). Statistical significance was set to ****$p < 0.001$. (H) Microscopic observations on inner surfaces of implants costained with FITC-WGA and PI. Scale bar = 200 μm.

within the biofilms on the inner implant microstructures was evaluated by using a bacterial CCK-8 assay kit following each treatment (Figure 3B). Compared to the PBS-treated group (0.68 ± 0.11), the CHX (0.40 ± 0.026) and SM+H_2O_2 (0.36 ± 0.013) groups showed significantly lower optical absorbance values (OD 450 nm) for solubilized orange-colored WST-8 formazan produced by living bacteria ($p < 0.0001$) (Figure 3B,C). There was no significant difference in absorbance between the CHX, SM + H_2O_2, and control group (without bacterial inoculation, 0.38 ± 0.021) ($p > 0.05$), indicating that both CHX and SM + H_2O_2 either completely removed or killed the bacteria (Figure 3C). In contrast, SEM images revealed that SM + H_2O_2 physically removed bacteria, as almost no bacteria remained on the inner implant microstructures (1.20 ± 1.79 bacteria/100 μm^2) (Figure 3D,E). However, treatments of CHX (79.80 ± 33.97) and H_2O_2 (80.60 ± 9.94) failed to remove bacteria from the surfaces, with no significant difference compared to the PBS-treated group (83.80 ± 21.02, $p > 0.05$), suggesting that dead bacteria were likely strongly adhered to the biofilm's EPS (Figure 3D,E). To evaluate the EPS removal efficiency of SM + H_2O_2 compared to conventional antiseptics, the internal spaces of implants were stained with FITC-conjugated wheat germ agglutinin (FITC-WGA) and imaged before and after each

https://doi.org/10.1021/acsbiomaterials.5c00303
ACS Biomater. Sci. Eng. 2025, 11, 3019−3030

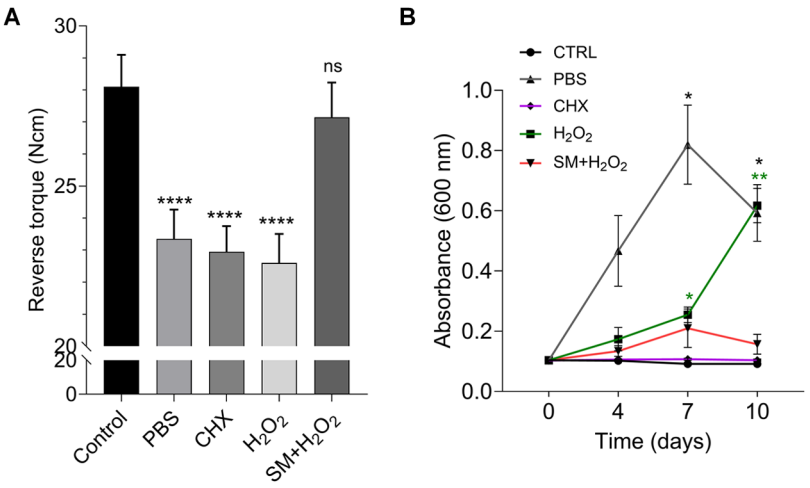

Figure 4. Reverse torque test and bacterial leakage test. (A) Reverse torque values for each group (n = 10). Data are expressed as average ± standard error of the mean (s.e.m.). Significance is set to ns, not specific; ****$p \leq 0.0001$. (B) Absorbance of the sterilized liquid broth containing each group at 600 nm is quantified (n = 4). Significance is set to *$p < 0.05$, **$p < 0.01$.

treatment. While the FITC signal intensity and area showed only marginal decreases following PBS, CHX, or H_2O_2 treatments, FITC signals were nearly undetectable in the SM + H_2O_2-treated group (Figure 3F,G). Microscopic observations of the inner surfaces of implants costained with FITC-WGA (for EPS) and PI (for dead bacteria) revealed that most bacteria were dead in the CHX-treated group, but the EPS remained intact (Figure 3H). In contrast, only a negligible amount of EPS and EPS-bound live or dead bacteria were detected in the SM + H_2O_2-treated group (Figure 3H). Next, we compared the efficacy of CHX and SM + H_2O_2 treatments in preventing recontamination. Following initial *P. gingivalis* contamination, the internal spaces of the implants were decontaminated using either CHX or SM combined with 3% H_2O_2. Subsequently, an equal amount of *P. gingivalis* was reseeded into the internal spaces. After 24 h, the degree of recontamination was assessed via crystal violet staining. Endoscopic images of the recontaminated implant internal spaces revealed that biofilm reformation occurred rapidly in the CHX-treated group, whereas it was significantly delayed in the SM + H_2O_2-treated group (Figure S3). These results suggest that effective prevention of recontamination requires not only bacterial elimination but also disruption of the extracellular polymeric substance (EPS) matrix.

Prevention of Mechanical Destabilization and Bacterial Leakage by Decontaminating Inner Implant Microstructures. As described above, contamination of the inner surfaces of implants can lead to clinical complications such as screw loosening and bacterial leakage. To determine whether SM + H_2O_2 treatment can address these issues, reverse torque measurements and bacterial leakage tests were performed after applying conventional antiseptics and SM + H_2O_2 to contaminated implant internal spaces. The mean reverse torque values of the PBS, CHX (22.95 ± 0.80 N cm), and H_2O_2-treated (22.60 ± 0.91 N cm) groups were significantly lower than those of the control group (28.10 ± 0.99 N cm) (Figure 4A). However, the mean reverse torque value of the SM + H_2O_2 group (27.15 ± 1.08 N cm) was significantly higher than those of the other groups and comparable to the control group ($p > 0.05$) (Figure 4A). For the bacterial leakage test, the bacterial population in the sterilized liquid broth incubated with PBS and H_2O_2-treated implants connected with abutments gradually increased and became noticeable by the 7th day (Figure 4B). However, only minimal bacterial growth was detected in the CHX and SM + H_2O_2-treated groups after 10 days of incubation, showing no significant difference from the control group (Figure 4B). These findings align with the previous results, which demonstrated that while conventional antiseptics kill bacteria without removing EPS, SM + H_2O_2 can achieve both.

Implant Internal Space Decontamination Efficiency of SM on Patient-Derived Samples. Next, we evaluated the decontamination efficiency of the SM in implant internal spaces under more clinically relevant conditions. Multispecies biofilms were collected from the inner implant microstructures of extracted peri-implantitis-affected implants and inoculated into the inner implant microstructures of sterilized implants. Each sample contained varying bacterial species compositions derived from different patients. The samples were stained with disclosing agents and treated with SM + H_2O_2. Endoscopic images of the implant spaces revealed that, regardless of the bacterial composition and degree of contamination (contaminated areas ranging from 24.40 to 62.63%), SM + H_2O_2 almost completely decontaminated the patient-derived multispecies biofilms on the inner surfaces of implants, with an average remaining contamination area of 1.87 ± 2.9% (Figure 5A,C). Finally, freshly extracted peri-implantitis-affected implants with varying internal structures and degrees of contamination were treated with SM + H_2O_2 to further assess the decontamination efficiency (Figure 5B). Regardless of implant types and contamination levels (contaminated areas ranging from 3.28 to 41.14%), a 300 s treatment with SM + H_2O_2 resulted in nearly complete decontamination of the internal spaces, with an average remaining contamination area of 0.18 ± 0.093% (Figure 5B,D).

Physicochemical Characteristics of the Titanium Disk Surface. Finally, we confirmed whether treatment of SM on implant internal space alters its physicochemical properties, including surface roughness and chemical composition. Surface roughness and chemical composition of implant internal space are critical for screw tightening, ensuring a robust connection between implant fixture and upper prosthesis. The R_a values of the H_2O_2 (0.12 ± 0.02 μm), DW + SM (0.12 ± 0.02 μm), and H_2O_2 + SM (0.13 ± 0.03 μm) groups were similar to those of

https://doi.org/10.1021/acsbiomaterials.5c00303
ACS Biomater. Sci. Eng. 2025, 11, 3019−3030

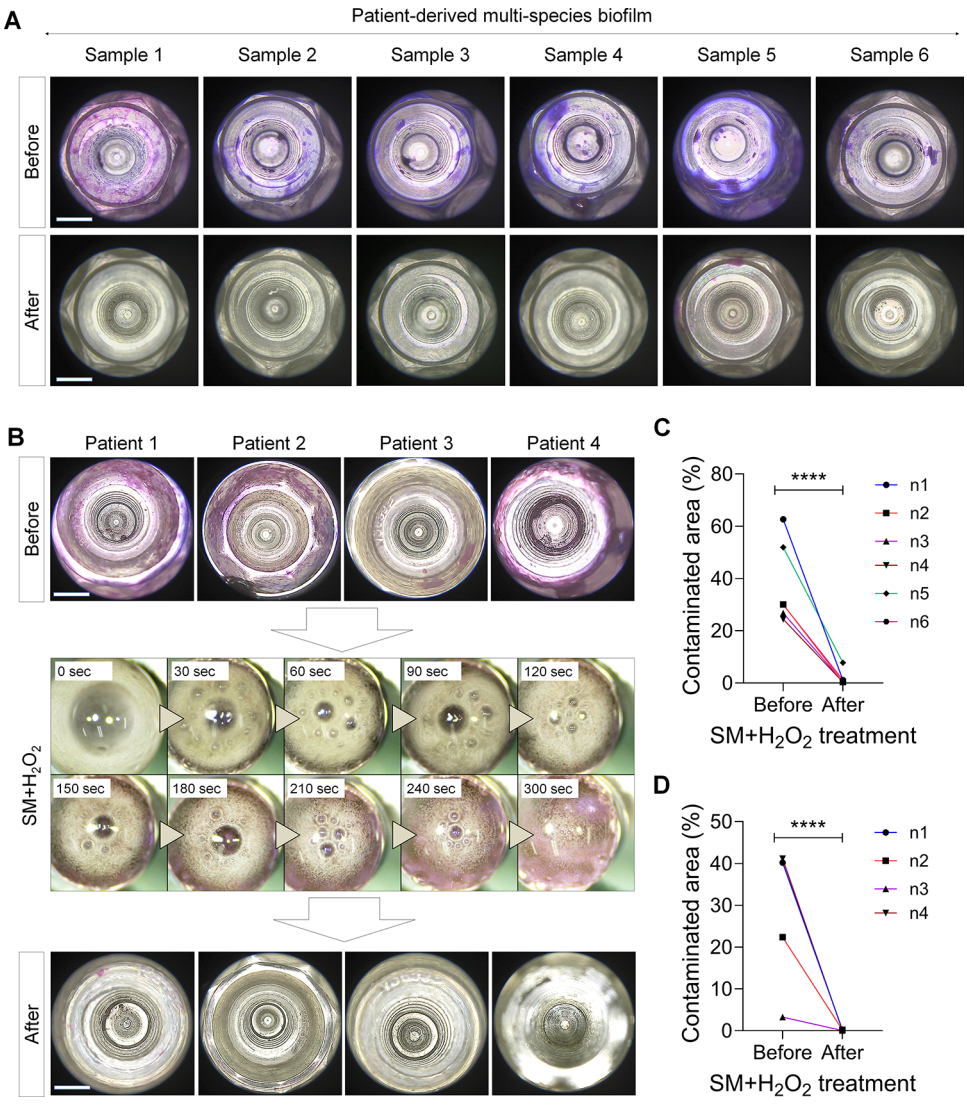

Figure 5. Endoscopic images of the multispecies biofilm within inner implant microstructure. (A) Endoscopic image of patient-derived multispecies biofilm removal test conducted on the inner surface of a sterilized implant using SM + H_2O_2. Scale bar = 2 mm. (B) Endoscopic image of patient-derived multispecies biofilm removal test conducted on the inner surface of an extracted implant using SM + H_2O_2. Time-lapse images of the decontamination process by SM for the first 300 s. Scale bar = 2 mm. (C) Quantification of the contaminated area in (A). Statistical significance was set to ****$p < 0.001$. (D) Quantification of the contaminated area in (B). Statistical significance was set to ****$p < 0.001$.

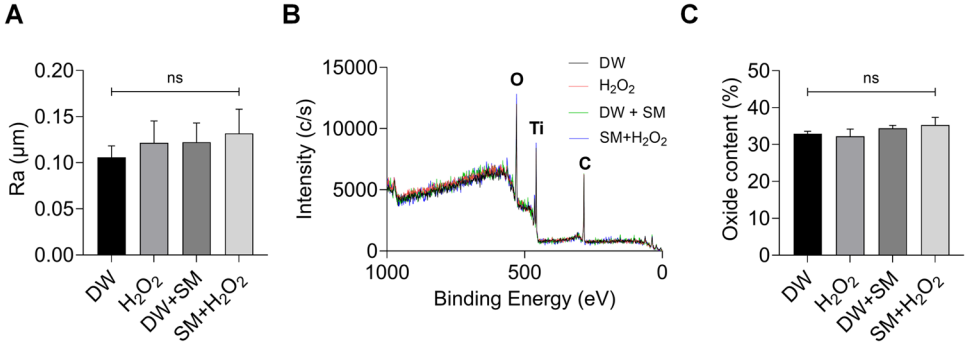

Figure 6. Physicochemical characteristics of the titanium disk surface after each treatment. (A) Average surface roughness (R_a) values of the titanium disks after each treatment. The data are presented as the mean value ± SD ($n = 4$). Significance is set to nanoseconds, not specific. (B) XPS results of the titanium disks obtained after each treatment. (C) Oxide contents of the titanium disks determined after each treatment. The data are presented as the mean value ± SD ($n = 4$). Significance is set to ns, not specific.

the DW-treated group (0.11 ± 0.01 μm), and no significant differences were observed (Figure 6A). An XPS analysis was conducted after each treatment to confirm whether any chemical modifications occurred. The XPS results indicated

https://doi.org/10.1021/acsbiomaterials.5c00303
ACS Biomater. Sci. Eng. 2025, 11, 3019−3030

that there was no significant chemical alteration occurred due to the treatment of H_2O_2, DW + SM, and H_2O_2 + SM. (Figure 6B). Additionally, the oxide contents of the H_2O_2 (32.23 ± 1.94%), DW + SM (34.39 ± 0.80%), and H_2O_2 + SM (35.31 ± 2.05%) groups were similar to those of the DW group (32.89 ± 0.71%) and no significant differences were observed (Figure 6C).

DISCUSSION

Peri-implantitis is a complex inflammatory condition that presents difficulties for patients and dentists. Studies indicate that bacteria can infiltrate the microgaps of the fixture-abutment interface (FAI) and form biofilms, a putative contributing factor in peri-implantitis relapse.[17−19] Our results from peri-implantitis-affected implants showed no significant difference in α and β diversity between the inner and outer implant surfaces, suggesting that bacteria can traverse the FAI microgaps, leading to a comparable microbiome. Similarly, Son et al. conducted 16s rRNA microbiome sequencing and found that the microbial compositions of the inner and outer implant surfaces in healthy subjects were alike.[20] Notably, over 60% of the bacterial genera identified on both surfaces were of the *Porphyromonas* species, and previous research also noted the presence of *P. gingivalis* within FAI microgaps. This finding implies that if not adequately decontaminated, the internal spaces of implants can serve as a pathogen reservoir causing peri-implant diseases.[21,22]

This study used innovative techniques tailored for examining implant internal space contamination. We used Trizol to extract bacterial nucleic acids from the entirety of the inner and outer implant surfaces. In contrast, many prior studies have used paper tips or microbrushes, allowing only partial sample collection from restricted areas.[9,20] Our approach to visualizing implant internal space using an ENT endoscope offers a pioneering method to inspect contamination directly. This study is the first attempt to examine biofilms inside the internal spaces of implants. The study used endoscopic visualization of agent-stained biofilms to observe variations in the contaminated regions across samples. For instance, the upper parts of the internal space were predominantly contaminated in samples from patients 1 and 2, whereas the lower region was extensively contaminated in the sample from patient 4 (Figure 5B). Previous studies focusing solely on the CFU of bacteria collected from limited areas of internal spaces using paper tips or microbrushes might not have captured these localized variations. Alongside endoscopic visualization, using artificial biofilms made of colored gelatin might aid in evaluating the efficacy of mechanical decontamination strategies. Our prior research found that the elastic modulus of peri-implantitis biofilms ranged from approximately 1208 to 1747 Pa, and 6% gelatin exhibited a similar modulus of 1300 Pa.[23] Our findings from the artificial biofilm removal assay indicate that decontaminating the bottom region of the internal space of implants poses more challenges than the top due to the buoyancy of oxygen bubbles produced by SM (Figure 1F,G). Notably, the catalytic activity of SM does not consistently increase with the concentration (Figure 1C−G). We suspect this result could be attributed to the immediate aggregation of SM particles upon exposure to an aqueous environment, leading to a significant decrease in surface-to-volume ratio.[24]

Our comprehensive comparison of decontamination efficacy with conventional antiseptics reveals that SM offers microlevel mechanical decontamination and bactericidal activity, whereas CHX or H_2O_2 provides only bactericidal action. Eliminating dead bacteria and biofilm EPS is critical as their endotoxins remain potent.[25] Any residual EPS structure can weaken the mechanical stability of implant abutment-fixture connection[26] and provide a niche for rehabilitation by newly infiltrated bacteria.[27]

The clinical application of SM in decontaminating implant internal spaces appears more promising than its use on external implant or tooth surfaces as the decontamination process occurs entirely within the implant, minimizing contact with oral tissues. SM-based cleaning technology effectively addresses the limitations of conventional methods for implant microgap decontamination. Physical cleaning is constrained by the narrow implant structure, while chemical antiseptics often encounter limited efficacy due to poor penetration. In contrast, SMs can propel into the biofilm, delivering mechanical disruption and oxygenation. This dual action—mechanical and chemical—enables more thorough biofilm removal by targeting both EPS and bacterial cells. This mechanism may also enhance the access and efficacy of antiseptics or antibiotics, helping to deactivate or eliminate bacteria that were previously protected within EPS. This approach is particularly beneficial for peri-implantitis patients as eliminating bacterial reservoirs within implants may help reduce reinfection risks. Beyond dental applications, SM technology has potential in orthopedic implants, where biofilm-related infections remain a major challenge.

Although the catalyzed chemical reactions of SM are proven to be biocompatible with oral mucosa,[23] its long-term toxicity remains unexamined. As depicted in Figure 5B, the reaction between 4 mg of SM and 20 μL of 3% H_2O_2 stays confined within the implant internal space. A rubber dam can prevent unanticipated contact with live tissue inundated with SM.

In conclusion, our findings propose that cotreatment with clinically available 3% H_2O_2 and SM can effectively remove biofilms formed inside dental implant internal spaces, resolve mechanical instability at the abutment-fixture connection, and prevent bacterial leakage. Furthermore, given that the implant internal space may harbor a microbiome similar to that of its external surface, the clinical importance of internal space decontamination deserves heightened attention.

CONCLUSIONS

In conclusion, this study demonstrates that the microbiomes of the outer and inner surfaces of implants affected by peri-implantitis are identical, confirming the hypothesis that the internal microstructures of implants can serve as bacterial reservoirs for peri-implantitis. To address this issue, we developed a nanozyme-doped diatom microbubbler (SM) capable of generating sufficient kinetic energy to dismantle biofilm structures embedded in the microstructures of implanted internal spaces. The combined application of 4 mg of SM and 3% H_2O_2 for 5 min effectively eliminated over 98% of biofilms composed of *P. gingivalis* or multispecies bacteria from peri-implantitis patients, significantly outperforming traditional antiseptics in decontamination efficacy. This SM treatment also improved the mechanical stability of the implant connection and prevented bacterial spread from the internal microstructures, all without damaging the implant surfaces.

This study introduces a simple, safe, cost-effective, and highly efficient SM-based strategy for biofilm decontamination, offering a novel maintenance solution for small and confined spaces within various biomedical devices.

https://doi.org/10.1021/acsbiomaterials.5c00303
ACS Biomater. Sci. Eng. 2025, 11, 3019−3030

■ ASSOCIATED CONTENT

Supporting Information

The Supporting Information is available free of charge at https://pubs.acs.org/doi/10.1021/acsbiomaterials.5c00303.

Photo of cross-sectioned fixture used in the experiment (Figure S1); photo of customized jig used in the experiment (Figure S2); and endoscopic images of recontaminated implant internal spaces following treatment of precontaminated surfaces with either chlorhexidine (CHX) or SM combined with 3% H_2O_2 (Figure S3) (PDF)

■ AUTHOR INFORMATION

Corresponding Authors

Hyunjoon Kong − *Departments of Chemical and Biomolecular Engineering, Scott H. Fisher Multi-Cellular Engineered Living System Theme, Carl R. Woese Institute for Genomic Biology, University of Illinois at Urbana−Champaign, Urbana, Illinois 61801, United States; Chan Zuckerberg Biohub Chicago, Chicago, Illinois 60642, United States;* orcid.org/0000-0003-4680-2968; Phone: +1-217-333-1178; Email: hjkong06@illinois.edu

Sang-woo Lee − *Department of Physiology, School of Dentistry and Dental Research Institute, Seoul National University, Seoul 03080, South Korea; Center for Nanoparticle Research, Institute for Basic Science (IBS), Seoul 08826, South Korea;* orcid.org/0000-0003-3950-6722; Phone: +82-2-740-8659; Email: goodman23@snu.ac.kr

Myung-Joo Kim − *Department of Prosthodontics, School of Dentistry and Dental Research Institute, Seoul National University, Seoul 110-749, South Korea;* orcid.org/0000-0003-2020-5284; Phone: +82-2-2027-0815; Email: silk1@snu.ac.kr

Authors

Eun-Hyuk Lee − *Department of Prosthodontics, School of Dentistry and Dental Research Institute, Seoul National University, Seoul 110-749, South Korea*

Hyunsub Kim − *Department of Prosthodontics, School of Dentistry and Dental Research Institute, Seoul National University, Seoul 110-749, South Korea*

Joo Hun Lee − *Departments of Chemical and Biomolecular Engineering, Scott H. Fisher Multi-Cellular Engineered Living System Theme, Carl R. Woese Institute for Genomic Biology, University of Illinois at Urbana−Champaign, Urbana, Illinois 61801, United States*

Youngjoon Kim − *Department of Physiology, School of Dentistry and Dental Research Institute, Seoul National University, Seoul 03080, South Korea;* orcid.org/0009-0008-0339-6430

Ho-Beom Kwon − *Department of Prosthodontics, School of Dentistry and Dental Research Institute, Seoul National University, Seoul 110-749, South Korea*

Young-Jun Lim − *Department of Prosthodontics, School of Dentistry and Dental Research Institute, Seoul National University, Seoul 110-749, South Korea*

Complete contact information is available at: https://pubs.acs.org/10.1021/acsbiomaterials.5c00303

Author Contributions

#E.-H.L. and H. Kim contributed equally to this work. E.-H.L: Investigation, data curation, formal analysis, methodology, writing—original draft; H. Kim: investigation, formal analysis, methodology, data curation, writing—original draft; J.H.L.: resources, formal analysis, and methodology; H. Kong: data curation and resources; Y.K.: writing—review & editing; H.-B.K.: methodology, writing—review & editing; Y.-J.L.: methodology, writing—review & editing; S.-w.L.: investigation, visualization, formal analysis, methodology, supervision, writing—review & editing; M.-J.K.: conceptualization, formal analysis, methodology, supervision, writing—review & editing. All authors approved the final manuscript and agree to be accountable for all aspects of the work.

Funding

This work was supported by the National Research Foundation of Korea (NRF) grant funded by the Korean Government (NRF-2018R1A5A2024418); Seoul National University Dental Hospital Research Fund 04-2021-0115 and 07-2023-0011; National Science Foundation (NSF-DMR 2004719); National Institute of Health (1R01AI160671-A1); Chan Zuckerberg Biohub Chicago Investigator Award; and the SerVaas Lab. acknowledgment.

Notes

The authors declare no competing financial interest.

■ ABBREVIATIONS

SM:diatom microbubbler; MnO_2:manganese oxide; H_2O_2:hydrogen peroxide; EPS:extracellular polymeric substances; FAI:fixture-abutment interface; CHX:chlorhexidine; SEM:scanning electron microscopy; EDS:energy-dispersive spectroscopy; PBS:phosphate-buffered saline; BHI:brain-heart infusion; CCK-8:cell counting kit-8; FITC:fluorescein isothiocyanate; PI:propidium iodide; CLSM:confocal laser scanning microscopy; RTV:reverse torque value; R_a:roughness average; XPS:X-ray photoelectron spectroscopy; OD:optical density; CFU:colony forming unit

■ REFERENCES

(1) Flemming, H.-C.; Wingender, J.; Szewzyk, U.; Steinberg, P.; Rice, S. A.; Kjelleberg, S. Biofilms: An Emergent Form of Bacterial Life. *Nat. Rev. Microbiol.* **2016**, *14* (9), 563−575.

(2) Townsend, E. M.; Moat, J.; Jameson, E. CAUTI's Next Top Model−Model Dependent Klebsiella Biofilm Inhibition by Bacteriophages and Antimicrobials. *Biofilm* **2020**, *2*, No. 100038.

(3) Tande, A. J.; Patel, R. Prosthetic Joint Infection. *Clin. Microbiol. Rev.* **2014**, *27* (2), 302−345.

(4) El-Chami, M. F.; Bonner, M.; Holbrook, R.; Stromberg, K.; Mayotte, J.; Molan, A.; Sohail, M. R.; Epstein, L. M. Leadless Pacemakers Reduce Risk of Device-Related Infection: Review of the Potential Mechanisms. *Heart Rhythm* **2020**, *17* (8), 1393−1397.

(5) Mello Dias, E. C. L. C.; Bisognin, E. D. C.; Harari, N. D.; Machado, S. J.; da Silva, C. P.; de Almeida Soares, G. D.; Vidigal, G. M., Jr. Evaluation of Implant-Abutment Microgap and Bacterial Leakage in Five External-Hex Implant Systems: An In Vitro Study. *Int. J. Oral Maxillofac. Implants* **2012**, *27* (2), 346−355.

(6) Golab, K. G.; Balouch, A.; Mirtorabi, S. One-Year Multicenter Prospective Evaluation of Survival Rates and Bone Resorption in One-Piece Implants. *Clin. Implant Dent. Relat. Res.* **2016**, *18* (2), 392−400.

(7) Li, X.; Sun, L.; Zhang, P.; Wang, Y. Novel Approaches to Combat Medical Device-Associated Biofilms. *Coatings* **2021**, *11* (3), 294.

(8) Carvalho, É. B. S.; Romandini, M.; Sadilina, S.; Sant'Ana, A. C.; Sanz, M. Microbiota Associated with Peri-Implantitis—A Systematic Review with Meta-Analyses. *Clin. Oral Implants Res.* **2023**, *34* (11), 1176−1187.

(9) Groenendijk, E.; Dominicus, J. J.; Moorer, W. R.; Aartman, I. H.; Van Waas, M. A. Microbiological and Clinical Effects of

Chlorhexidine Enclosed in Fixtures of 3I-Titamed Implants. *Clin. Oral Implants Res.* **2004**, *15* (2), 174−179.
(10) Jervøe-Storm, P. M.; Hablützel, A. S.; Bartels, P.; Kraus, D.; Jepsen, S.; Enkling, N. Comparison of Irrigation Protocols for the Internal Decontamination of Dental Implants—Results of In Vitro and In Vivo Studies. *Clin. Oral Implants Res.* **2021**, *32* (10), 1168−1175.
(11) Gonzalez, I.; Wong, X.; DeAlmeida, D.; Yurko, R.; Watkins, S.; Islam, K.; Montelaro, R.; El-Ghannam, A.; Mietzner, T. Peptides as Potent Antimicrobials Tethered to a Solid Surface: Implications for Medical Devices. *Nat. Precedings* **2008**, *1*, 1.
(12) Roque-Borda, C. A.; Duran Gleriani Primo, L. M.; Medina-Alarcón, K. P.; Campos, I. C.; Nascimento, C. F.; Saraiva, M. M. S.; Berchieri, Â.; Fusco-Almeida, A. M.; Soares Mendes-Giannini, M. J.; Perdigão, J.; Pavan, F. R.; Alberício, F. Antimicrobial Peptides: A Promising Alternative to Conventional Antimicrobials for Combating Polymicrobial Biofilms. *Adv. Sci.* **2025**, *12* (1), No. 2410893.
(13) Hwang, G.; Paula, A. J.; Hunter, E. E.; Liu, Y.; Babeer, A.; Karabucak, B.; Stebe, K.; Kumar, V.; Steager, E.; Koo, H. Catalytic Antimicrobial Robots for Biofilm Eradication. *Sci. Robot.* **2019**, *4* (29), No. eaaw2388.
(14) Yuan, Z.; Tao, B.; He, Y.; Mu, C.; Liu, G.; Zhang, J.; Liao, Q.; Liu, P.; Cai, K. Remote Eradication of Biofilm on Titanium Implant via Near-Infrared Light Triggered Photothermal/Photodynamic Therapy Strategy. *Biomaterials* **2019**, *223*, No. 119479.
(15) Seo, Y.; Leong, J.; Park, J. D.; Hong, Y. T.; Chu, S. H.; Park, C.; Kim, D. H.; Deng, Y. H.; Dushnov, V.; Soh, J.; Rogers, S.; Yang, Y. Y.; Kong, H. Diatom Microbubbler for Active Biofilm Removal in Confined Spaces. *ACS Appl. Mater. Interfaces* **2018**, *10* (42), 35685−35692.
(16) Cho, W. R.; Huh, Y. H.; Park, C. J.; Cho, L. R. Effect of Cyclic Loading and Retightening on Reverse Torque Value in External and Internal Implants. *J. Adv. Prosthodont.* **2015**, *7* (4), 288−293.
(17) Sasada, Y.; Cochran, D. L. Implant-Abutment Connections: A Review of Biologic Consequences and Peri-implantitis Implications. *Int. J. Oral Maxillofac. Implants* **2017**, *32* (6), 1296−1307.
(18) Harder, S.; Dimaczek, B.; Açil, Y.; Terheyden, H.; Freitag-Wolf, S.; Kern, M. Molecular Leakage at Implant-Abutment Connection—In Vitro Investigation of Tightness of Internal Conical Implant-Abutment Connections Against Endotoxin Penetration. *Clin. Oral Invest.* **2010**, *14*, 427−432.
(19) Lauritano, D.; Moreo, G.; Lucchese, A.; Viganoni, C.; Limongelli, L.; Carinci, F. The Impact of Implant−Abutment Connection on Clinical Outcomes and Microbial Colonization: A Narrative Review. *Materials* **2020**, *13* (5), 1131.
(20) Son, M.; Song, Y.; Yu, Y.; Kim, S. Y.; Huh, J. B.; Bae, E. B.; Cho, W. T.; Na, H. S.; Chung, J. The Oral Microbiome of Implant-Abutment Screw Holes Compared with the Peri-Implant Sulcus and Natural Supragingival Plaque in Healthy Individuals. *J. Periodontal Implant Sci.* **2023**, *53* (3), 233.
(21) do Nascimento, C.; Miani, P. K.; Pedrazzi, V.; Gonçalves, R. B.; Ribeiro, R. F.; Faria, A. C. L. Leakage of Saliva through the Implant-Abutment Interface: In Vitro Evaluation of Three Different Implant Connections under Unloaded and Loaded Conditions. *Int. J. Oral Maxillofac. Implants* **2012**, *27* (3), 551−560.
(22) Callan, D. P.; Cobb, C. M.; Williams, K. B. DNA Probe Identification of Bacteria Colonizing Internal Surfaces of the Implant-Abutment Interface: A Preliminary Study. *J. Periodontol.* **2005**, *76* (1), 115−120.
(23) Lee, E. H.; Lee, S. W.; Seo, Y.; Deng, Y. H.; Lim, Y. J.; Kwon, H. B.; Park, K.; Kong, H.; Kim, M. J. Antimicrobial Efficacy of Self-Locomotive Manganese Oxide Nanozyme-Doped Diatom Microbubbler on Orthodontic Brackets In Vitro. *BMC Oral Health* **2023**, *23* (1), 33.
(24) Deng, Y.-H.; Ricciardulli, T.; Won, J.; Wade, M. A.; Rogers, S. A.; Boppart, S. A.; Flaherty, D. W.; Kong, H. Self-Locomotive, Antimicrobial Microrobot (SLAM) Swarm for Enhanced Biofilm Elimination. *Biomaterials* **2022**, *287*, No. 121610.
(25) Cavaillon, J. M. Exotoxins and Endotoxins: Inducers of Inflammatory Cytokines. *Toxicon* **2018**, *149*, 45−53.
(26) Prado, A. M.; Pereira, J.; Henriques, B.; Benfatti, C. A.; Magini, R. S.; López-López, J.; Souza, J. C. Biofilm Affecting the Mechanical Integrity of Implant-Abutment Joints. *Int. J. Prosthodont.* **2016**, *29* (4), 381−383.
(27) Liu, Y.; Wang, J. Influences of Microgap and Micromotion of Implant−Abutment Interface on Marginal Bone Loss around Implant Neck. *Arch. Oral Biol.* **2017**, *83*, 153−160.

https://doi.org/10.1021/acsbiomaterials.5c00303
ACS Biomater. Sci. Eng. 2025, 11, 3019−3030